Journal of Radiation Research and Applied Sciences 18 (2025) 101910

Contents lists available at ScienceDirect

Journal of Radiation Research and Applied Sciences

journal homepage: www.journals.elsevier.com/journal-of-radiation-research-and-applied-sciences

Radioactivity and aeromagnetic of magmatic suites, Arabian Nubian Shield: Petrological and health risk characteristics

El Saeed R. Lasheen [a,*], Basma A. El-Badry [b], Waheed H. Mohamed [a], Ghada A. Khouqeer [b], Ioan V. Sanislav [c], Mabrouk Sami [d]

[a] Geology Department, Faculty of Science, Al-Azhar University, Cairo, 11884, Egypt
[b] Physics Department, Faculty of Science, Imam Mohammad Ibn Saud Islamic University (IMSIU), Riyadh, 11564, Saudi Arabia
[c] Economic Geology Research Centre (EGRU), College of Science and Engineering, James Cook University, Townsville, QLD, 4811, Australia
[d] Geosciences Department College of Science, United Arab Emirates University, 15551, Al Ain, United Arab Emirates

ARTICLE INFO

Keywords:
Radiological risks
Granitic phases
Magnetic anomaly
And structural mapping

ABSTRACT

This study attempts to assess radiation doses in the El Maghrabiya- Ria Elgarra granitic phases and elucidate the subsurface structural influences on mineralization employing sophisticated airborne magnetic data processing and interpretation methods. The granitic phases include granodiorite, monzogranites, syenogranites, and altered granites (which are frequently visible along shear zones). The former rocks show a small amount of ^{238}U (21.70 ± 11.87 Bqkg^{-1}), ^{232}Th (20.20 ± 12.78 Bqkg^{-1}), and ^{40}K (305.18 ± 168.1 Bqkg^{-1}) employing the NaI (Tl) spectrometer. Monzogranites contain ^{238}U (43.40 ± 41.13 Bqkg^{-1}), ^{232}Th (29.29 ± 5.08 Bqkg^{-1}), and ^{40}K (1169.84 ± 79.45 Bqkg^{-1}), while syenogranites include high amounts of ^{238}U (121.52 ± 46.73 Bqkg-1), ^{232}Th (96.15 ± 12.58 Bqkg^{-1}), and ^{40}K (1315.23 ± 146.62 Bqkg^{-1}). Furthermore, the altered granites had the greatest activity of ^{232}Th (105.04 ± 65.73 Bqkg^{-1}), ^{40}K (683.91 ± 333.34 Bqkg^{-1}), and ^{238}U (1674.00 ± 1275.25 Bqkg^{-1}), alongside the total quantity (avg. 1842.90 ± 871.02 Bqkg^{-1}). Several radiological elements have been utilized to assess the risk inherent with these rocks. Granodiorite and monzogranite results are consistent with established global standards, however syenogranites and altered granites exhibited elevated metrics. Therefore, granodiorite and monzogranite are suitable for use in the construction sector, whereas syenogranites and altered granites are unsuitable due to their elevated natural gamma radiation emissions. Upward continuation was subsequently applied to RTP aeromagnetic data at four discrete levels (0.5 km, 1 km, 2 km, and 3 km), corresponding to average source depths, to image subsurface geological structures. Based on automated lineament extraction methods and rose diagrams, the principal structural directions are N-S, NNW-SSE, and E-W. The identification of these trends as the dominant structural trends is not just a descriptive finding; it reveals the fundamental plumbing system of the region. These trends are the highways and intersections along which mineralizing fluids traveled and where they were most likely to deposit their economic metal load.

1. Introduction

Radionuclide spectrum are crucial in tracking natural radioactivity because of the regional variance in external gamma dose rates. These dosages are established by the quantity of radionuclides that spontaneously reside in rocks (Al-Hamarneh & Awadallah, 2009; Krebs et al., 2019; Yıldırım & Gülmez, 2025). Radium's existence has no effect on long-term processes since it is constantly generated and has a relatively short half-life, which is caused by the decay of ^{232}Th, ^{238}U, and ^{238}U (Kanmi et al., 2025; Ramola et al., 2011). According to Akkurt and Günoğlu (2014), the Earth's crust contains natural radionuclides that have been present since the planet's formation, including substantial amounts of ^{232}Th, ^{238}U, and ^{40}K. However, as rocks have varying degrees of the ability to move, the disequilibrium among uranium and radium occurs regularly (Lei et al., 2023; Li et al., 2015; Yuan et al., 1995). The processes of deposition and weathering are frequent processes that progressively boost radionuclides, especially in the latter stages of granitic rocks and phosphorites. In this regard, U has been demonstrated to combine with organic matter and phosphates (Fathy et al., 2023; Kanmi et al., 2025; Wais et al., 2023), and Th has been

* Corresponding author.
E-mail address: elsaeedlasheen@azhar.edu.eg (E.S.R. Lasheen).

https://doi.org/10.1016/j.jrras.2025.101910
Received 15 July 2025; Received in revised form 8 August 2025; Accepted 24 August 2025
Available online 28 August 2025

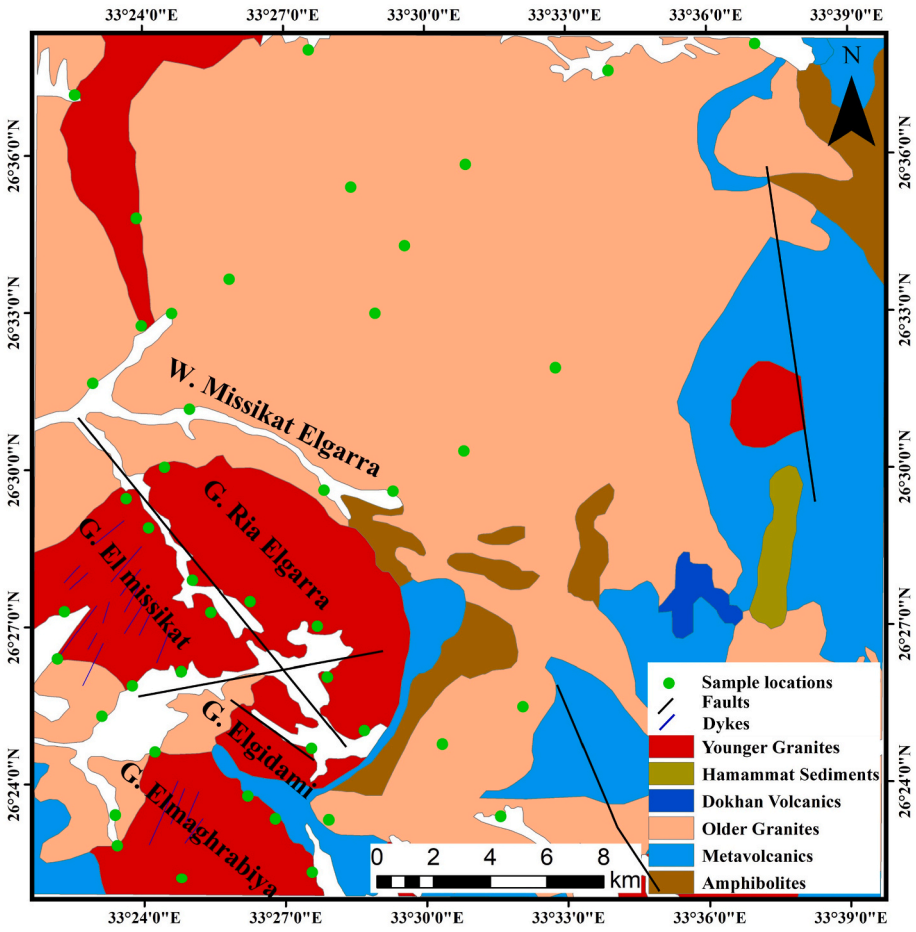

Fig. 1. El Maghrabiya- Ria Elgarra geologic map, Central Eastern Desert, Egypt (modified after Elhussein et al., 2024; Shereif et al., 2025).

found to mix with clay-rich sediments. This geological differentiation causes the establishment of discrete high-radiation zones, that could stay dormant unless disturbed by natural erosion or human activity including mining or hydraulic fracturing. The link of sedimentary rock lithology and migration of radionuclides highlights the difficulties in predicting and describing the corresponding threats (Abdel-Aal et al., 2024; Qureshi et al., 2014; Raghavendra et al., 2019; Özden et al., 2023).

In the past few decades, there has been an increased emphasis on following the natural dispersion of radioactive materials. Several research projects have been initiated worldwide to determine the entire radiation intensity of the rocks (Abdul Sani et al., 2022; Akkurt & Günoğlu, 2014; Al-Hamarneh & Awadallah, 2009; Al-Mur et al., 2025; AlZahrani et al., 2011; Khaleal et al., 2023; Li et al., 2015, 2024; O'Brien & Sanna, 1976; Ravisankar et al., 2015; Sahoo et al., 2011; Sayyed et al., 2024; Shahrokhi et al., 2020; Shehzad et al., 2019; Vukasinovic et al., 2010; Wais et al., 2025; Özden & Aközcan, 2021).

Mineral exploration faces the persistent challenge of efficiently detecting economically viable deposits concealed beneath complex geology and often obscured by surface covers. Geophysical methods provide indispensable tools for probing the subsurface, with airborne magnetic surveying standing as a particularly powerful and cost-effective technique for regional-scale investigations. The fundamental physical property measured, magnetic susceptibility, exhibits significant contrasts between various rock types, particularly those rich in magnetite or other ferromagnetic minerals, and their altered or mineralized counterparts. Consequently, the interpretation of magnetic data offers critical insights into lithological variations, structural frameworks, and hydrothermal alteration systems, which represent the key that control the emplacement and distribution of mineral deposits (Elhussein et al., 2024; Khalifa et al., 2024).

This study focuses on applying advanced airborne magnetic data processing and interpretation techniques to elucidate the subsurface structural controls on mineralization within the study area. Additionally, is to identify rock units through fieldwork and petrography, and to analyze the radioactive potential of the El Maghrabiya- Ria Elgarra rocks. This analysis involves measuring the ^{232}Th, ^{238}U, and ^{40}K radiation in these rocks. Furthermore, various radiological risk parameters are evaluated to assess the potential adverse effects of radiation exposure on human health and assess their ability for uses in construction sector.

2. Field geology

Neoproterozoic rocks are frequently observed in the Eastern Desert, Arabian Nubian Shield, which occupying 10 % of Egypt's surface area (Saleh et al., 2024; Stern, 2018). They possesses rock varieties like ophiolites, arc-related, granitic suites, and Dokhan Volcanics. Furthermore, the bulk of these rocks survived the ore mining; they can be utilized for building parts in cement as well as stones for ornamentation due to their attractive forms and remarkable strength (Lasheen et al., 2023, 2024). Granite is a particularly widespread rock in the crust of the earth, accounting for 60 % of the Nubian Shield. These rocks are extremely segregated and include commercial and crucial components such as Li, Ta, REEs, Nb, and Sn (Khan et al., 2025; Lasheen et al., 2025; Saleh, Kamar, et al., 2025; Stern, 2018).

El Maghrabiya- Ria Elgarra is located in the center sector of Egypt's Eastern Desert. It has a multitude of granitic rocks (Fig. 1). The overall

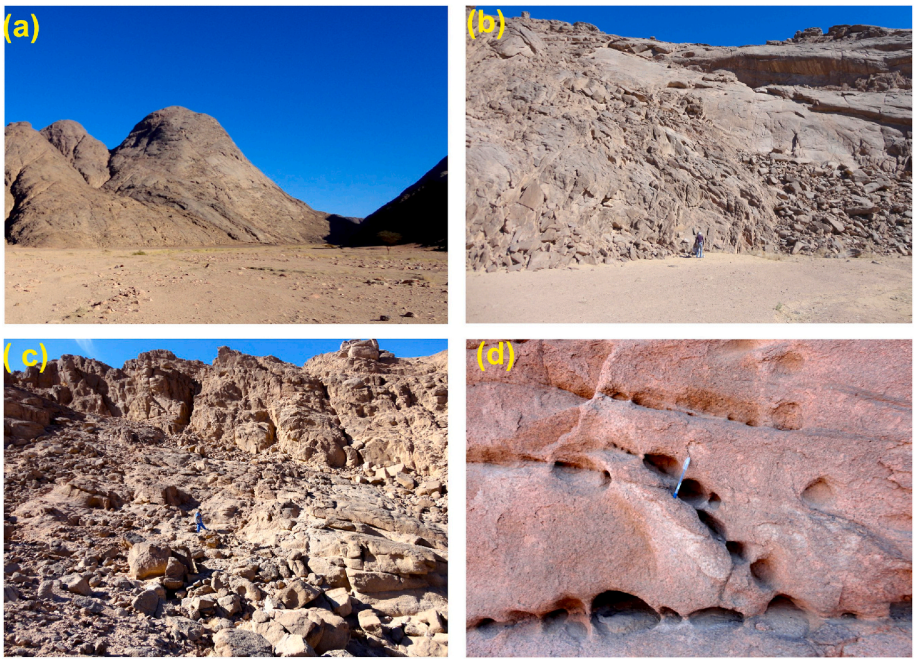

Fig. 2. Field photos show: **a)** General view of numerous oval peaks of younger granites; **b**) Smooth surface as a result of weathering products; **c**) Fractured granites showing boulder weathering; **d**) Small oriented cavernous in younger granites.

geography of the examined area ranges from mild to harsh, and has many peaks. Red granite usually possess prominent peaks (Fig. 2a). Older granites are distinguished by whitish grey with darker grey tints, medium-to coarse-grained, exfoliated with a pore-like and boulders shape along their edges. They are readily weathered and cracked, resulting in low terrains, making it difficult to obtain a fresh rock sample. They are invaded by younger granites and primarily divided by fundamental dikes. Younger granites are one of the prominent rock units in the study area. They range from pink to reddish and have medium-grained rocks. They are the most prominent elevation changes, with oval and rounded shapes. They comprise xenoliths of all sizes and forms that originate from previous rocks (Abdel-Hakeem et al., 2023). They exhibit cavernous weathering with diverse diameters ranging from 2 cm to 1 m (Fig. 2b–d). They sometimes demonstrate vertical jointing and exfoliation as a result of weathering that takes place.

3. Methodology

3.1. Field and petrography

More than forty samples have been gathered from El Maghrabiya-Ria Elgarra area (including mountains of El Maghrabiya, El Missikat, Ria Elgarra, and El Gidami) randomly from all granitic phases, which include older granites (16), and younger granites (26) through one field trip. The altered granites possesses those gathered from El Missikat area (Supplementary materials). Eleven thin sections were, created to recognize the essential mineralogical and their texture.

3.2. Radioactive detection

Seventeen rock specimens (~400 g each) from the El Maghrabiya-Ria Elgarra outcrops were air-dried, sieved to <200 mesh, placed in 200 mL plastic containers, and sealed for 4 weeks to establish radioactive equilibrium. Gamma-ray measurements were carried out with a Bicron NaI(Tl) spectrometer equipped with a 76 × 76 mm scintillation crystal and a photomultiplier tube in an aluminum housing (Supplementary materials). Activity was evaluated in three energy windows: 92.6 keV (^{234}Th, used to quantify ^{238}U), 238.6 keV (^{212}Pb, used to quantify ^{232}Th), and 1460.8 keV (for ^{40}K). Minimum detectable is ~0.4 ppm for U, 0.6 ppm Th, and 0.1 % K, with counting uncertainties of 1–5 %. Accuracy is maintained by rigorous energy-calibration procedures that correct for possible peak interferences. To evaluate the radiological consequences of samples, employ the next formulas: D_{air}, rate of absorbed dose; R_{aeq}, radium equivalent; Hγ, gamma index; ELCR, excess life-time cancer; $AED_{out\ \&\ in}$ outdoor and indoor annualized dosage; and H_{ex} & H_{in} internal and external indicators. ^{232}Th, ^{40}K, ^{238}U, and activity are designated as H_{Th}, H_K, and H_U, respectively (European Commission, 1999; European Commission, 1999; Taskin et al., 2009; UNSCEAR, 2010; UNSCEAR, 2010; UNSCEAR, 2010; UNSCEAR, 2010; Yu et al., 1992).

$$D_{air}\left(nGyh^{-1}\right) = 0.430H_U + 0.666H_{Th} + 0.042H_K \quad (1)$$

$$Ra_{eq}\left(Bqkg^{-1}\right) = H_U + 1.43\,H_{Th} + 0.077\,H_K \quad (2)$$

$$I\gamma = H_U/300 + H_{Th}/200 + H_K/3000 \quad (3)$$

$$AED\left(\frac{mSv}{y}\right) = \sum\left(D_{air}\left(\frac{nGy}{h}\right) \times 0.7\left(\frac{Sv}{Gy}\right) \times occupancy\ factor\right) \times 8760h \times 10^{-6} \quad (4)$$

where, the occupancy factor accounts for occupancy time in case outdoor is 0.2 and indoor 0.8

$$ELCR(mSv/y) = AED\ x\ DL\ (70\ years) x\ RF\ \left(0.05\ Sv^{-1}\right) \quad (5)$$

$$H_{ex\ \&}\ H_{in=}\ H_U/370\ (H_U/185\ for\ indoor) + H_{Th}/259 + H_K/4810 \quad (6)$$

3.3. Airborne magnetic data

The utility of airborne magnetic data in mineral exploration stems from its ability to rapidly map large areas, penetrating through superficial covers like vegetation, soil, and recent sediments to image magnetic contrasts within the bedrock (Ahmed et al., 2025; Elhussein et al., 2024). Total Magnetic Intensity (TMI) data, acquired by aircraft equipped with magnetometers, captures the spatial variation of the Earth's magnetic field influenced by the underlying geology. The

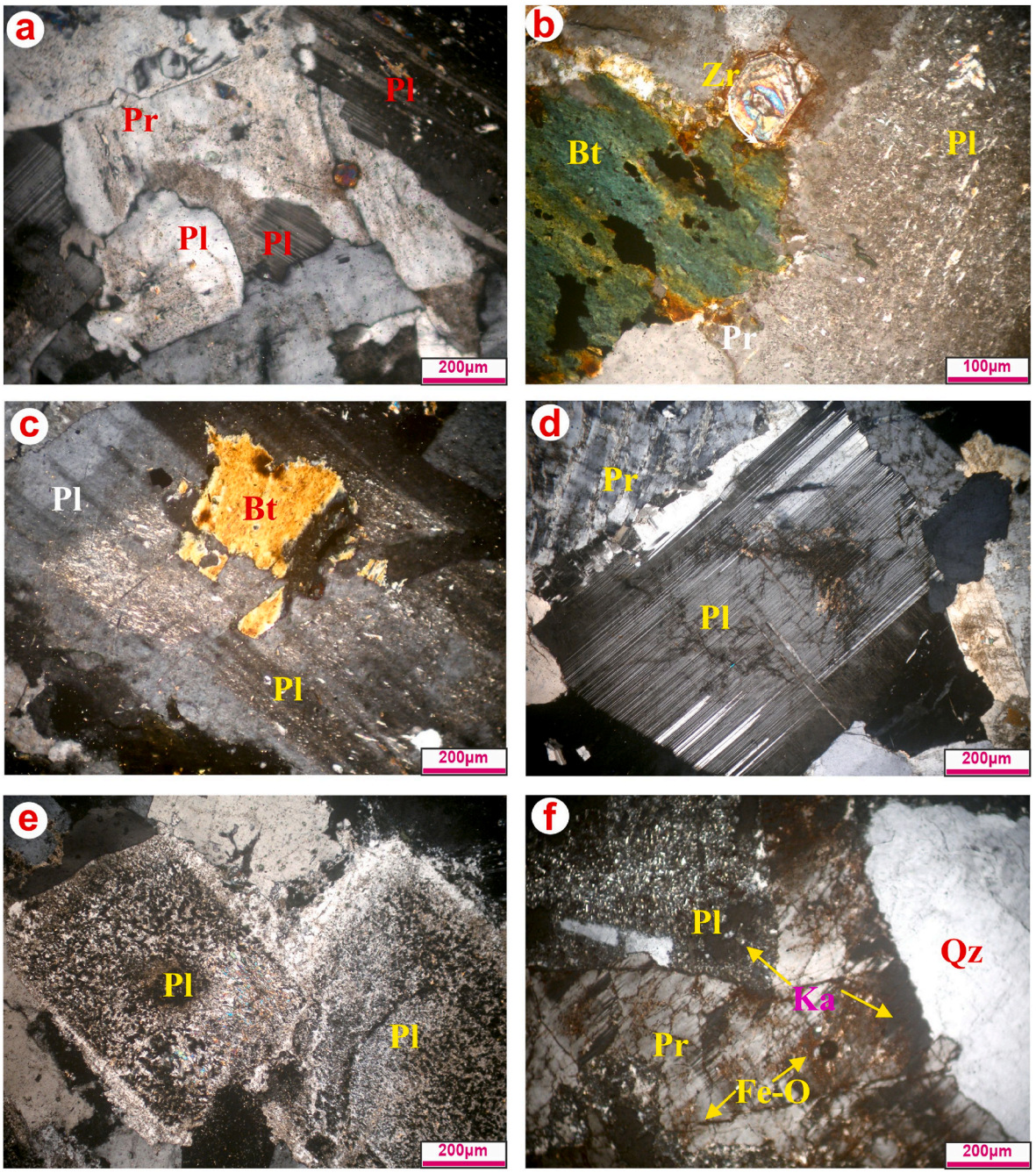

Fig. 3. Microscopic photomicgraphs reveal: **a**) Kaolinitized perthite (Pr) corroded by plagioclase (Pl); **b**) Euhedral zircon (Zr) associated with chloritized biotite (Bt); **c**) Saussuritized plagioclase enclosing biotite; d) Slightly pristine albitic plagioclase; e) Completely saussuritized plagioclase with dusty surface; and f) Stained perthite by iron oxide (Fe-O) and kaolinite (Ka), which corroded by quartz (Qz).

traverse flight lines were aligned in a northeast–southwest direction with a spacing of 1.5 km, while the tie lines were oriented perpendicularly in a northwest–southeast direction and spaced at 5 km intervals. The ground clearance of about 120 m (Aero-Service, 1984). However, raw TMI anomalies in the study area are inherently complex, representing the vector superposition of induced and remnant magnetization within rocks, further complicated by the inclination and declination of the Earth's magnetic field. These factors cause anomalies to appear offset and asymmetrical relative to their causative sources, particularly at non-polar latitudes. To overcome this limitation and produce a magnetic map where anomalies are centered directly over their sources, thereby simplifying geological interpretation, Reduction to the Magnetic Pole (RTP) is routinely applied using (IGRF = 42425 nT, Inclination = 32.8N, Declination = 1.9E) (Baranov & Naudy, 1964).

This crucial transformation (RTP) corrects for the dipolar nature of the magnetic field, effectively simulating the anomaly pattern as if measured at the magnetic pole where the field is vertical.

3.3.1. *Upward continuation*

Beyond correcting for field geometry, isolating structural information often requires enhancing signals related to deeper geological features. Upward Continuation is a potent filtering technique employed for this purpose. It mathematically transforms the measured magnetic field at the flight altitude to simulate the field that would be measured at a higher elevation. This process inherently acts as a low-pass filter, attenuating high-frequency anomalies associated with shallow, small-

Table 1
^{232}Th, ^{40}K, and ^{238}U activity concentration and their ratios of the assessed rocks.

Rock types	Samples	^{232}Th (Bqkg^{-1})	^{40}K (Bqkg^{-1})	$^{232}Th/^{40}K$	^{238}U (Bqkg^{-1})	$^{232}Th/^{238}U$
Granodiorite	**G1**	16.16	241.01	0.07	12.40	1.30
	G2	4.04	109.55	0.04	12.40	0.33
	G3	32.32	500.80	0.06	24.80	1.30
	G4	28.28	369.34	0.08	37.20	0.76
	Min.	4.04	109.55	0.04	12.40	0.33
	Max.	32.32	500.80	0.08	37.20	1.30
	Avg.	20.20	305.18	0.06	21.70	0.92
	SD	12.78	168.10	0.02	11.87	0.47
Monzogranites	**M1**	28.28	1270.78	0.02	12.40	2.28
	M2	24.24	1101.76	0.02	49.60	0.49
	M3	28.28	1111.15	0.03	12.40	2.28
	M4	36.36	1195.66	0.03	99.20	0.37
	Min.	24.24	1101.76	0.02	12.40	0.37
	Max.	36.36	1270.78	0.03	99.20	2.28
	Avg.	29.29	1169.84	0.03	43.40	1.35
	SD	5.08	79.45	0.00	41.13	1.07
Syenogranites	**S1**	105.04	1302.08	0.08	124.00	0.85
	S2	92.92	1167.49	0.08	111.60	0.83
	S3	84.84	1176.88	0.07	173.60	0.49
	S4	84.84	1458.58	0.06	49.60	1.71
	S5	113.12	1471.10	0.08	148.80	0.76
	Min.	84.84	1167.49	0.06	49.60	0.49
	Max.	113.12	1471.10	0.08	173.60	1.71
	Avg.	96.15	1315.23	0.07	121.52	0.93
	SD	12.58	146.62	0.01	46.73	0.46
Altered granites	**A1**	68.68	1139.32	0.06	917.60	0.07
	A2	60.60	688.60	0.09	3310.80	0.02
	A3	88.88	554.01	0.16	446.40	0.20
	A4	202.00	353.69	4.96	2021.20	0.10
	Min.	60.60	353.69	0.06	446.40	0.02
	Max.	202.00	1139.32	4.96	3310.80	0.20
	Avg.	105.04	683.91	1.32	1674.00	0.10
	SD	65.73	333.34	2.43	1275.25	0.08

Table 2
Comparison of ^{238}U, ^{40}K, and ^{232}Th of the El Maghrabiya- Ria Elgarra rocks with others.

Location	^{238}U (Bqkg^{-1})	^{226}Th (Bqkg^{-1})	^{40}K (Bqkg^{-1})	Reference
Nigeria, Irepodun	5.42	3.07	735.24	Kanmi et al. (2025)
Egypt	137.00	82.00	1082.00	Sharaf and Hamideen (2013)
Serbia	200	77	1280	((Kuzmanović et al., 2024)
Saudi Arabia	28.82	34.83	665.08	AlZahrani et al. (2011)
India	25.88	42.82	560.60	Senthilkumar et al. (2014)
Sharm El Luli, Egypt	24.57	23.32	241.83	Saleh, Lasheen, et al. (2025)
Jeddah shoreline	13.14	5.05	139.09	Al-Mur et al. (2025)
China	356	318	1636	Tuo et al. (2020)
Wadi El Gemal Island	12.49	12.63	325.13	(Khaleal et al., 2023)
Spain	84	42	1138	Guillén et al. (2014)
Egypt	137	82	1082	Amin (2012)
	33	45	412	UNSCEAR (2010)
Granodiorite	21.70	20.20	305.18	Current study
Monzogranites	43.40	29.29	1169.84	
Syenogranites	121.52	96.15	1315.23	
Altered granites	1674.00	105.04	683.91	

scale sources (like near-surface lithological variations or cultural noise) while preserving and enhancing lower-frequency anomalies originating from deeper, larger-scale structures (such as faults, shear zones, basement trends, and intrusive contacts). By applying upward continuation to the RTP data, the resultant maps provide a clearer depiction of the fundamental structural grain, basement architecture, and major tectonic lineaments that frequently act as primary controls on fluid pathways and mineral deposition within the study area (Hamimi et al., 2023; Osinowo & Taiwo, 2020). The transformation was implemented computationally within the frequency domain using Fourier transform methods to derive the necessary coefficients. Processing was conducted at four discrete elevation levels, corresponding to average source depths of 0.5 km, 1 km, 2 km, and 3 km, by adjusting the computational grid spacing parameters. This generate four resultant magnetic anomaly maps (Fig. 6) for the specified continuation levels. This integrated approach – transforming raw TMI data via RTP and subsequently applying upward continuation – forms the core methodology for constructing a robust model of the subsurface structural framework to guide targeted mineral exploration efforts. This reductions and process of magnetic data was carried out using the Oasis Montaj™ software version 7.1 (Phillips, 2007).

3.3.2. *Structural features*

The Centre for Exploration Targeting (CET) grid analysis is a powerful image processing technique used for enhancing structural and lithological features within potential field data, particularly magnetic datasets (Abdelhakim Eshanibli, 2020; Holden et al., 2012). When applied to upward continued magnetic grids, this method facilitates the identification of subtle geological features that may not be readily visible in the raw or shallow-depth data. Upward continuation serves to suppress high-frequency noise and near-surface anomalies, thereby emphasizing deeper, more regional magnetic sources. Within this context, the CET grid analysis employs a combination of texture analysis and bilateral symmetric feature detection algorithms to enhance linear and curvilinear features associated with subsurface structures (Abdelhakim Eshanibli, 2020; Eshanibli et al., 2021). One of its core

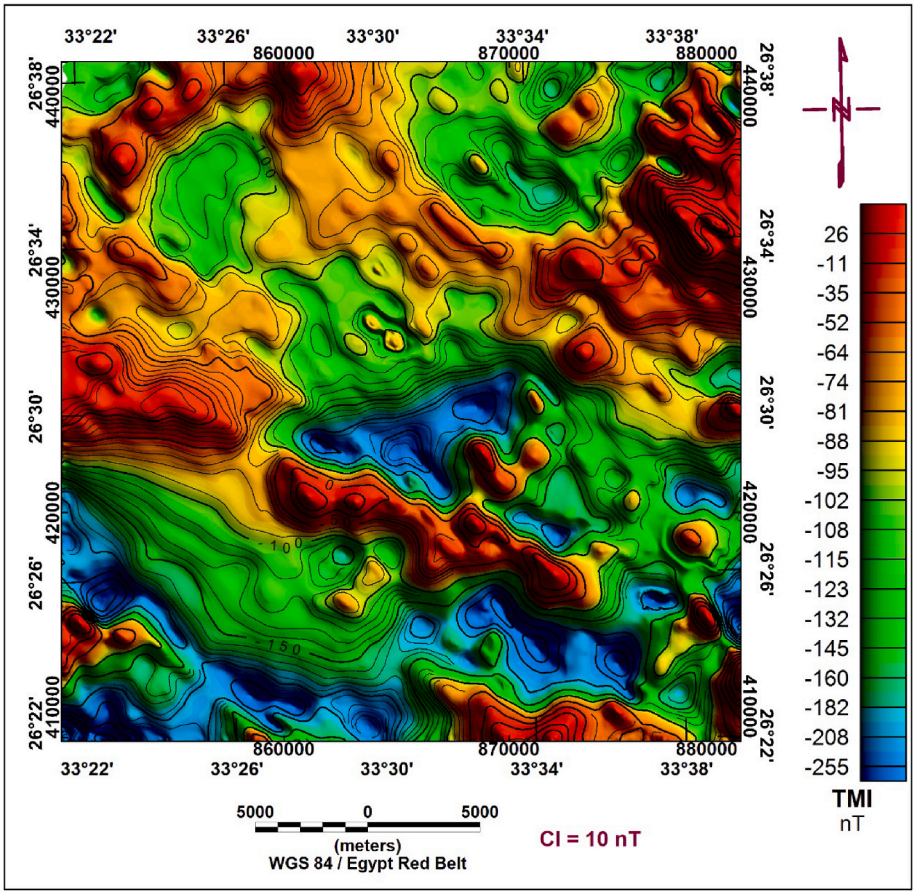

Fig. 4. Total aeromagnetic intensity map (TMI) of the study area.

operations involves calculating the local standard deviation of grid values across a moving window. This computation quantifies the local variability of magnetic intensity, with higher standard deviation values indicating abrupt changes or discontinuities—often linked to geological boundaries, fault zones, or lithological contacts. Compared to the smoother background signal, these zones of high variability are interpreted as regions of structural significance. By detecting such density discontinuities and enhancing textural contrasts, the CET analysis significantly improves the ability to delineate structural frameworks, which is critical for mineral exploration and geological interpretation.

4. Results

4.1. Petrography

Mineralogical and textural analyses have been conducted for granodiorite, monzogranite, syenogranite, and altered granite varieties. The granodiorite primarily comprises plagioclase, quartz, K-feldspar, and biotite as essential constituents, with zircon and iron oxides present as accessory phases. Plagioclase (An_{22-30}) is the most abundant mineral, accounting for approximately 41–73 % of the total composition. It typically appears as euhedral to subhedral tabular crystals exhibiting well-developed lamellar and carlsbad twinning and is locally altered to saussurite and kaolinite (Fig. 3a). Quartz grains show pronounced undulose extinction and are frequently fractured, with cracks filled by iron oxides and sericite. Potassium feldspar is mainly represented by perthitic orthoclase, occurring as subhedral to anhedral crystals with characteristic patchy to flame perthitic textures as an intergrown with plagioclase. Biotite forms anhedral, flaky crystals and often displays variable degrees of chloritization (Fig. 3b). Zircon appears as well-formed euhedral crystals, typically associated with biotite and plagioclase.

Monzogranite has a medium-grained, hypidiomorphic texture. Quartz appears as anhedral crystals in these rocks, resulting in wavy extinction and/or mortar texture. Plagioclase (An_{5-20}) appears as subhedral prismatic crystals, the majority of which have been converted to saussurite (Fig. 3c). Microcline and perthite form coarse anhedral platy crystals. It is converted to kaolinite. It is broken and filled with sericite and iron oxides. They produce intergrowth with quartz to provide micrographic texture. Biotite is a yellowish brown subhedral flaky crystal that converts into chlorite, in particular near its cleavage. A few of these biotite crystals contain scattered iron oxides.

The remarkably common minerals in syenogranites are orthoclase (prevailing) and microcline-perthite. They contain quartz, biotite, and plagioclase in a poikilitic formation. The patchy form of perthite is prevalent. Albite (An_{6-13}) exists in pure form (Fig. 3d), ranging from euhedral to subhedral, and occasionally shows small modifications to saussurite. Quartz is less common than perthite, which occurs as medium anhedral crystals (sometimes as skeletal crystals in albite). Muscovite appears as uneven flakes. Zircon is defined as a short minute with strong relief. Radiogenic processes have resulted in significant pleochroic haloes surrounding some zircon crystals.

The altered granites have the same composition of syenogranites, but the rock constituents are mainly transformed to other secondary minerals. Albite and perthite are completely converted to saussurite and kaolinite, respectively (Fig. 3e and f).

4.2. Radionuclides abundance

The prevalence and levels of radioactive elements ^{232}Th, ^{40}K, and ^{238}U have been determined for seventeen samples collected from the El Maghrabiya- Ria Elgarra area (Table 1). The average ± SD results of

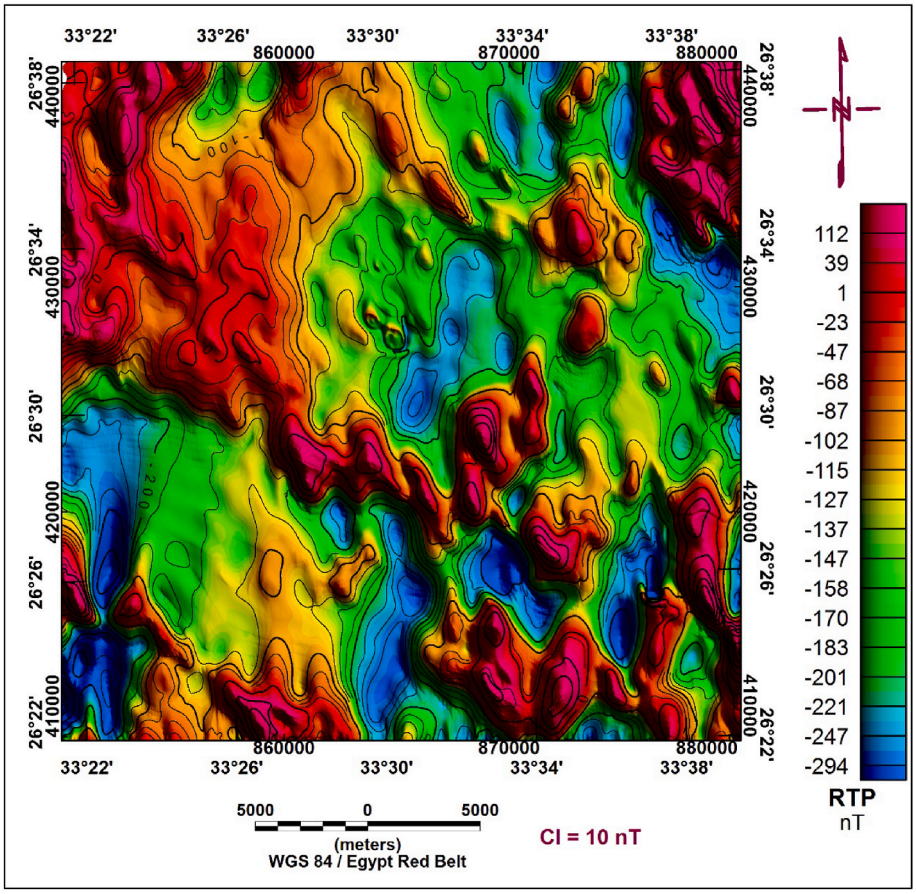

Fig. 5. The reduced to the northern magnetic pole (RTP) map derived from aeromagnetic Field Intensity Map of the study area.

granodiorite and monzogranites rocks are within the global record limit (45 for ^{232}Th, 412 for ^{40}K, and 33 for ^{238}U accordingly UNSCEAR (2010). In reality, the samples obtained from the El Maghrabiya- Ria Elgarra area exhibit a progression of their degree of activity, as illustrated here (Table 1): ^{40}K > ^{238}U > ^{232}Th, which corresponds to strongly rocks (with high SiO_2 levels and potash-bearing minerals) that have a connection with higher K activity (Abdel-Aal et al., 2024; Abdul Sani et al., 2022; Freitas & Alencar, 2004; Shahrokhi et al., 2020; Zakaly et al., 2024).

Applying the NaI (Tl) analyzer, granodiorite has ^{238}U (21.70 ± 11.87 Bqkg^{-1}), ^{232}Th (20.20 ± 12.78 Bqkg^{-1}), and ^{40}K (305.18 ± 168.1 Bqkg^{-1}), meanwhile monzogranites have higher ^{238}U (43.40 ± 41.13 Bqkg^{-1}), ^{232}Th (29.29 ± 5.08 Bqkg^{-1}), and ^{40}K (1169.84 ± 79.45 Bqkg^{-1}). Contrary to this, syenogranites and altered granites have radioactive amounts that exceed the global recording limit. Syenogranite contains ^{238}U (121.52 ± 46.73 Bqkg^{-1}), ^{232}Th (96.15 ± 12.58 Bqkg^{-1}) and ^{40}K (1315.23 ± 146.62 Bqkg^{-1}). Whilst granodiorite has the lowest activities, the altered granites have the highest activity concentrations of ^{232}Th (105.04 ± 65.73 Bqkg^{-1}), ^{40}K (683.91 ± 333.34 Bqkg^{-1}), and ^{238}U (1674.00 ± 1275.25 Bqkg^{-1}), as well as their summation (avg. 1921.15 ± 844.57 Bqkg^{-1}). These increased of these concentrations could be due to the existence of radioactive minerals such as zircon, thorite, allanite, and titanite, which incorporate radionuclides within their structure (Freitas & Alencar, 2004; Kanmi et al., 2025; Li et al., 2024; Pavlidou et al., 2006; Sahoo et al., 2011; Sivakumar et al., 2018; UNSCEAR, 2010; Vukasinovic et al., 2010).

Table 1 demonstrates that altered granites have the highest ^{232}Th/^{40}K (average 0.22), above the worldwide limit of 0.07 (Qureshi et al., 2014). This could be attributed to the high potassium abundance in these rocks as a result of K-metasomatism (Al-Mur et al., 2025; Lasheen et al., 2021). The altered granites exhibit a low ^{232}Th/^{238}U ratio (avg. 0.1), compared to the global average of 3.94 (Qureshi et al., 2014). The smallest observations are connected with a high U level in contrast to Th in the tested samples, demonstrating U migration in relation to Th in changed granites. This is due to secondary U accumulation throughout hydrothermal activity (Abdel-Aal et al., 2024; Kanmi et al., 2025; Khandaker et al., 2025; Qureshi et al., 2014; UNSCEAR, 2000).

Table 2 compares the findings of the present inquiry (^{232}Th, ^{40}K, and ^{238}U) with the average concentration of those obtained from other countries. Granodiorite and monzogranite activity concentration fall within the permissible quantity of UNSCEAR (2010) (Table 2), and are comparable to others like those of Saudi Arabia phosphorite (AlZahrani et al., 2011), Jeddah coastline (Al-Mur et al., 2025), Sharm El Luli coastline (Saleh, Lasheen, et al., 2025), Wadi El- Gemal sediments (Khaleal et al., 2023), commercial granitic rocks (Sharaf & Hamideen, 2013), flooring materials (Senthilkumar et al., 2014), and Sapin granites (Guillén et al., 2014). Controversy, other rocks including syenogranites and altered granites have ^{232}Th, ^{40}K, and ^{238}U akin to those of Amin (2012), Kuzmanović et al. (2024), and Tuo et al. (2020) and higher than the permissible quantity of UNSCEAR (2010).

4.3. Magnetic data interpretation

4.3.1. The Total Magnetic Intensity map

The Total Magnetic Intensity (TMI) map (Fig. 4) depicts spatial variations in the Earth's magnetic field across the study area, utilizing a color gradient from deep blue (−255 nT) to bright red/pink (26 nT) to delineate magnetic intensity. High-amplitude anomalies dominate the northeastern, northwestern and central parts, these anomalies often appear as elongated or irregular shapes, suggesting underlying magnetic sources, while low-intensity anomalies (blue/purple/green colors) are prevalent in southern, central and northern regions, frequently forming

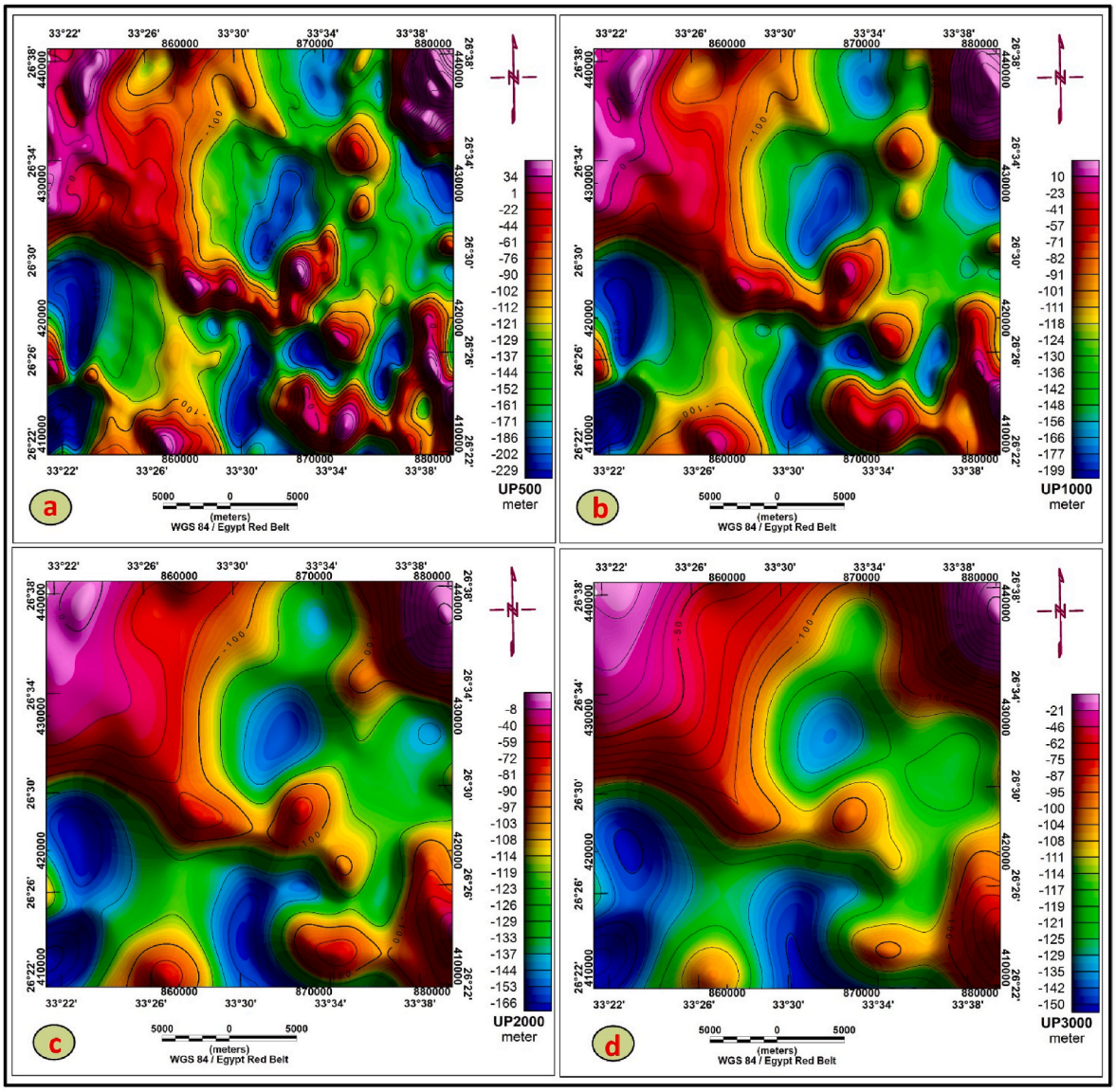

Fig. 6. Upward continuation map to (a) 500 m, (b) 1000m, (c) 2000m, and (d) 3000m of aeromagnetic data in the study area.

peripheries to high-anomaly zones. Gradient analysis reveals steep contours indicating rapid transitions in magnetic intensity (implying shallow or strongly magnetized bodies) versus widely spaced contours reflecting gradual shifts (consistent with deeper or weakly magnetized sources) (Zhdanov, 2015).

4.3.2. *The Reduced to the pole*

The Reduced to the Pole (RTP) magnetic map (Fig. 5), correcting anomalies to simulate a vertical inducing field, facilitates source body localization (Baranov & Naudy, 1964; Hao et al., 2018). It reveals a pronounced spatial correlation between high-amplitude magnetic anomalies (112 nT) concentrated in the northwestern, northeastern and southeastern and outcrops of granodiorite and metavolcanics (Fig. 1). This correlation is attributable to their high magnetic susceptibility, derived from magnetite content. Elongated heights align with mapped Dikes, interpreted as magnetically susceptible mafic intrusive. Conversely, extensive low-magnitude anomalies (−294 nT) correlate strongly with low-susceptibility unit of felsic rocks (e.g., monzogranites and syenogranites, which mask deeper sources. Sharp magnetic gradients delineate structural features, notably coinciding with Thrust Faults, Fracture Lineaments, and geologic contacts, indicating susceptibility contrasts arising from fault juxtaposition or lithological boundaries. Anomaly morphology further supports geological interpretation: linear highs suggest structurally controlled intrusive bodies (dykes/sills), while circular/irregular highs potentially indicate discrete intrusions (plugs/stocks) or mineralized zones.

4.3.3. *Upward continuation*

The upward continuation maps illustrate how magnetic anomalies vary with height, where at 500 m (Fig. 6a) high-frequency, short-wavelength anomalies with sharp gradients dominate, indicating shallow sources such as lithological contacts, faults, dykes, or small magnetic bodies. At 1000 m (Fig. 6b), the anomalies appear smoother with reduced amplitude, and intermediate wavelengths become more prominent, suggesting moderately deep sources while some shallow features remain visible but with less clarity, indicating their limited vertical extent. At 2000 m (Fig. 6c), the maps are characterized by broad, long-wavelength anomalies representing deeper crustal structures like basement undulations, large intrusions, or major structural trends, with near-surface noise largely diminished to reveal the regional tectonic framework. At 3000 m (Fig. 6d), anomalies are further smoothed, dominated by very long wavelengths that reflect the deepest

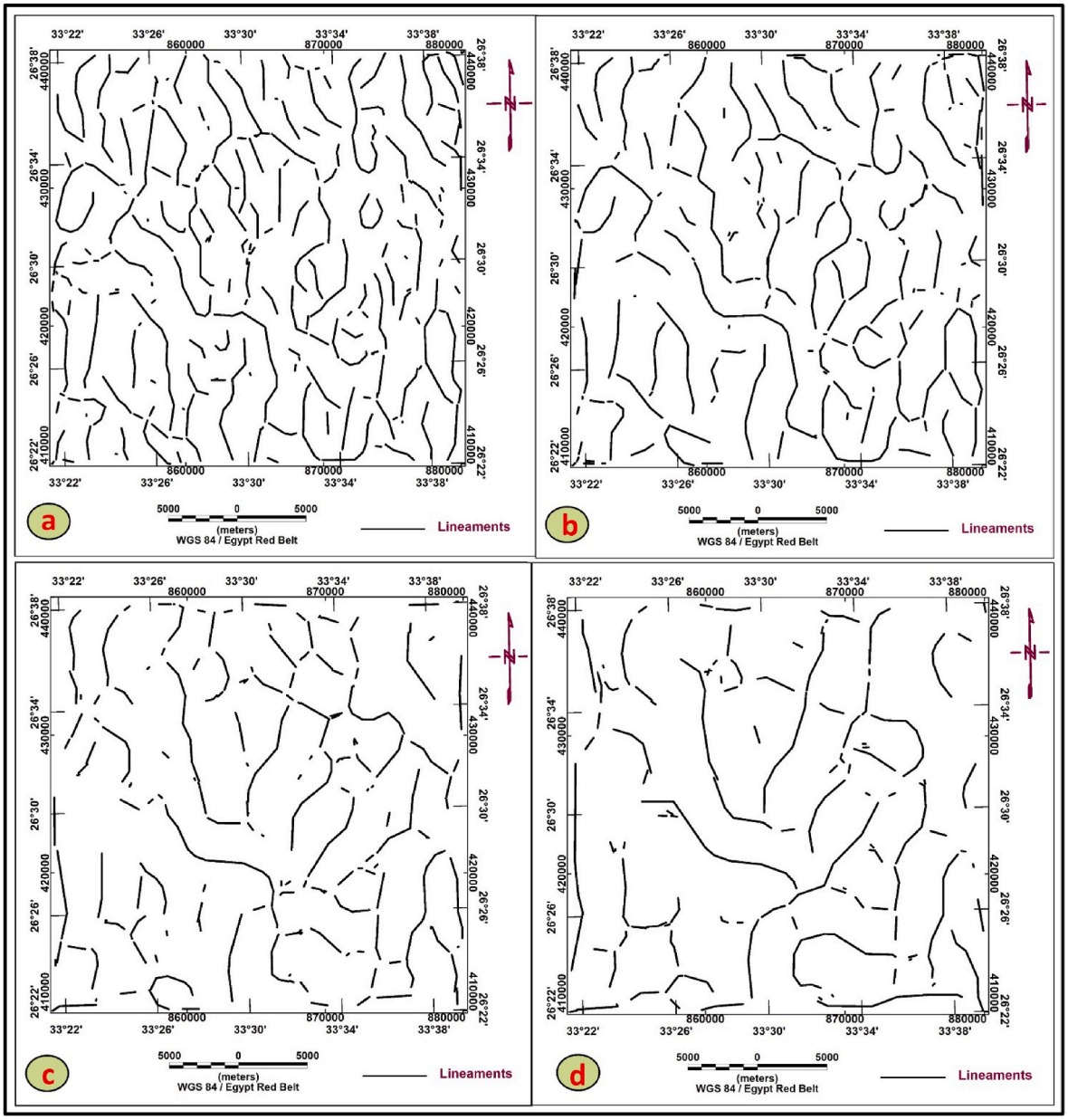

Fig. 7. Automated lineament Extraction maps showing the subsurface structural lineaments that deduced from the upward continuation (a) 500 m, (b) 1000 m, (c) 2000 m, and (d) 3000 m of aeromagnetic data in the study area.

and most extensive sources such as major crustal lineaments and regional tectonic features, while shallow anomalies are fully suppressed.

4.3.4. *Structural mapping*

The lineament maps (Fig. 7) derived from upward continued magnetic data at 500 m, 1000 m, 2000 m, and 3000 m (Fig. 6) illustrate the structural architecture of the study area at different depths. At 500 m (Fig. 7a), the map shows a dense network of short, closely spaced lineaments trending in multiple directions, primarily N-S, NNW-SSE, NW-SE, and NE-SW, indicating a complex near-surface fracture system. At 1000 m(Fig. 7b), many of the smaller feature's fade, and more continuous lineaments begin to dominate, particularly along N-S, NNW-SSE, NW-SE trends. At 2000 m (Fig. 7c), the lineaments are fewer and longer, showing a clearer structural grain aligned mostly in the N-S, NNW-SSE, and NE-SW directions, which become even more dominant and regionally extensive at 3000 m (Fig. 7d). This progression reveals a transition from local, shallow structural features to deep-seated, crustal-scale tectonic zones. The N-S and NNW-SSE trend, consistently present and becoming more prominent with depth, is likely the primary structural control in the area.

5. Discussion

5.1. *Radiation risk impact*

The AED $_{\text{out \& in}}$, D_{air}, Iγ, ELCR, H_{ex}, H_{in}, and R_{aeq} are numbers of indicators that have been utilized to assess the radioactivity El Maghrabiya- Ria Elgarra outcrops (Table 3).

As outlined by Kumar et al. (2024) and UNSCEAR (2000), the D_{air} aspect serves as a key parameter for evaluating the intensity of terrestrial gamma radiation at a height of the Earth over a meter. The tested samples had D_{air} measurements ranging from 35.60 ± 19.53 (granodiorite) to 815.21 ± 546.16 nGyh^{-1} (altered granites). Among the investigated lithologies, granodiorite exhibited D_{air} values fall within the

Table 3
Radiological parameters of the El Maghrabiya- Ria Elgarra rocks.

Rock types	Samples	Dair nGyh^{-1}	H_{in}	H_{ex}	Iγ	AED_{out} (mSvy^{-1})	AED_{in} (mSvy^{-1})	R_{aeq}	ELCR
Granodiorite	**G1**	26.22	0.18	0.15	0.20	0.03	0.13	54.07	0.11
	G2	12.62	0.11	0.07	0.10	0.02	0.06	26.61	0.05
	G3	53.22	0.36	0.30	0.41	0.07	0.26	109.58	0.23
	G4	50.34	0.39	0.29	0.39	0.06	0.25	106.08	0.22
	Min.	12.62	0.11	0.07	0.10	0.02	0.06	26.61	0.05
	Max.	53.22	0.39	0.30	0.41	0.07	0.26	109.58	0.23
	Avg.	35.60	0.26	0.20	0.28	0.04	0.17	74.08	0.15
	SD	19.53	0.14	0.11	0.15	0.02	0.10	40.57	0.08
Monzogranites	**M1**	77.54	0.44	0.41	0.61	0.10	0.38	150.69	0.33
	M2	83.75	0.59	0.46	0.65	0.10	0.41	169.10	0.36
	M3	70.83	0.41	0.37	0.55	0.09	0.35	138.40	0.30
	M4	117.09	0.93	0.66	0.91	0.14	0.57	243.26	0.50
	Min.	70.83	0.41	0.37	0.55	0.09	0.35	138.40	0.30
	Max.	117.09	0.93	0.66	0.91	0.14	0.57	243.26	0.50
	Avg.	87.30	0.59	0.47	0.68	0.11	0.43	175.36	0.37
	SD	20.55	0.24	0.13	0.16	0.03	0.10	46.99	0.09
Syenogranites	**S1**	177.96	1.35	1.01	1.37	0.22	0.87	374.47	0.76
	S2	158.91	1.20	0.90	1.23	0.19	0.78	334.37	0.68
	S3	180.58	1.51	1.04	1.40	0.22	0.89	385.54	0.78
	S4	139.09	0.90	0.76	1.08	0.17	0.68	283.23	0.60
	S5	201.11	1.55	1.14	1.55	0.25	0.99	423.84	0.86
	Min.	139.09	0.90	0.76	1.08	0.17	0.68	283.23	0.60
	Max.	201.11	1.55	1.14	1.55	0.25	0.99	423.84	0.86
	Avg.	171.53	1.30	0.97	1.32	0.21	0.84	360.29	0.74
	SD	23.50	0.26	0.14	0.18	0.03	0.12	53.59	0.10
Altered granites	**A1**	5.46	2.98	4.59	3.78	0.60	2.39	1103.54	2.10
	A2	18.27	9.33	16.55	11.57	1.83	7.32	3450.48	6.41
	A3	2.87	1.66	2.23	2.12	0.34	1.35	616.16	1.18
	A4	11.78	6.32	10.11	7.87	1.25	5.00	2337.29	4.37
	Min.	2.87	1.66	2.23	2.12	0.34	1.35	616.16	1.18
	Max.	18.27	9.33	16.55	11.57	1.83	7.32	3450.48	6.41
	Avg.	9.60	5.07	8.37	6.33	1.00	4.02	1876.87	3.51
	SD	6.89	3.45	6.38	4.24	0.67	2.69	1274.84	2.35

globally accepted safety of 59 nGyh^{-1}, as recognized by UNSCEAR (2010). In contrast, altered granites displayed significantly elevated D_{air} values, ranging from 274.41 to 1492.92 nGyh^{-1}, highlighting their pronounced radiological impact relative to other rock types in the study (Table 3).

The D_{air} results, along with a dose conversion factor of 0.7 Sv·Gy^{-1} and occupancy factors of 0.2 for outdoor and 0.8 for indoor environments, were utilized to estimate the annual effective dose for both outdoor (AED_{out}) and indoor (AED_{in}) exposure scenarios. The granodiorite exhibited mean AED_{out} readings 0.04 ± 0.02 mSvy^{-1}, remaining well below the internationally recommended limit (0.07 mSvy^{-1}; UNSCEAR, 2010). In contrast, monzogranites yielded average values close to the permissible limit, at 0.11 ± 0.03 mSvy^{-1} (UNSCEAR, 2010). Notably, syenogranites and altered granites possesses the highest results (0.21 ± 0.03; 1.0 ± 0.67, respectively). A similar trend is observed in the AED_{in} values for the assed rocks when compared with internationally recommended level (0.41 mSvy^{-1};O'Brien & Sanna, 1976; UNSCEAR, 2000).

The Iγ values for granodiorite and monzogranite are 0.28 ± 0.15 and 0.68 ± 0.15, respectively, both falling within the internationally recommended level of unity. In contrast, syenogranites and altered granites exhibit significantly elevated Iγ values, averaging 1.23 ± 0.18 and 6.33 ± 4.24, respectively, which exceed the recommended limit (Qureshi et al., 2014).

As a result, gamma-ray exposure influences both the R_{aeq} and the internal and external alpha emissions. The estimated mean Raeq values for granodiorite (74.08 ± 40.57 Bqkg^{-1}), monzogranite (175.36 ± 46.99 Bqkg^{-1}), and syenogranite (360.29 ± 53.59 Bqkg^{-1}) remain within the internationally recommended level of 370 Bqkg^{-1} (Yu et al., 1992). However, altered granites exhibit substantially higher Raeq values, ranging from 616.16 to 3450.48 Bqkg^{-1}, with a mean of 1876.87 ± 1274.84 Bqkg^{-1}, far exceeding the internationally recommended outlined by (UNSCEAR, 2010).

The H_{in} and H_{ex} hazard factors are widely utilized to assess the potential risks to human health (Sayyed et al., 2024; UNSCEAR, 2010). The calculated mean H_{in} and H_{ex} values for granodiorite (0.89 ± 0.17) and monzogranite (0.65 ± 0.11) fall below the internationally recommended safety limit (1; UNSCEAR, 2010), indicating minimal radiological concern. In contrast, syenogranites show elevated values with 1.3 ± 0.26 for H_{in} and 0.97 ± 0.14 for H_{ex}), approaching or slightly exceeding the permissible limits. Altered granites present the highest hazard, with mean H_{in} and H_{ex} values of 9.6 ± 6.89 and 5.07 ± 3.44, respectively, signaling significant radiological risks (Attallah et al., 2018; European Commission, 1999; Shahrokhi et al., 2020; Wais et al., 2023; Özden et al., 2023).

The estimated ELCR for granodiorite averages 0.015 ± 0.08 × 10^{-3}, remaining well below the recommended safety limit (0.029 × 10^{-3} Qureshi et al. (2014). In comparison, monzogranite exhibits a mean ELCR of 0.37 ± 0.09 × 10^{-3}, approaching the permissible limit. Conversely, syenogranites and altered granites show significantly elevated ELCR values of 0.74 ± 0.10 × 10^{-3} and 3.51 ± 2.35 × 10^{-3}, respectively, which are substantially over the allowable level. All the investigated rocks have ELCR values below those of the granitic rocks (avg. 633 10^{-3}) (Awad et al., 2020). These findings indicate a potentially increased risk of cancer for individuals exposed to syenogranites and altered granites over a prolonged period of close contact (O'Brien & Sanna, 1976; UNSCEAR, 2000).

As previously noted, the radiological characteristics of the analyzed samples follow an increasing risk trend in the order: granodiorite < monzogranite < syenogranite < altered granite.

5.2. Structural setting

The elongation of RTP magnetic anomalies and alignment of

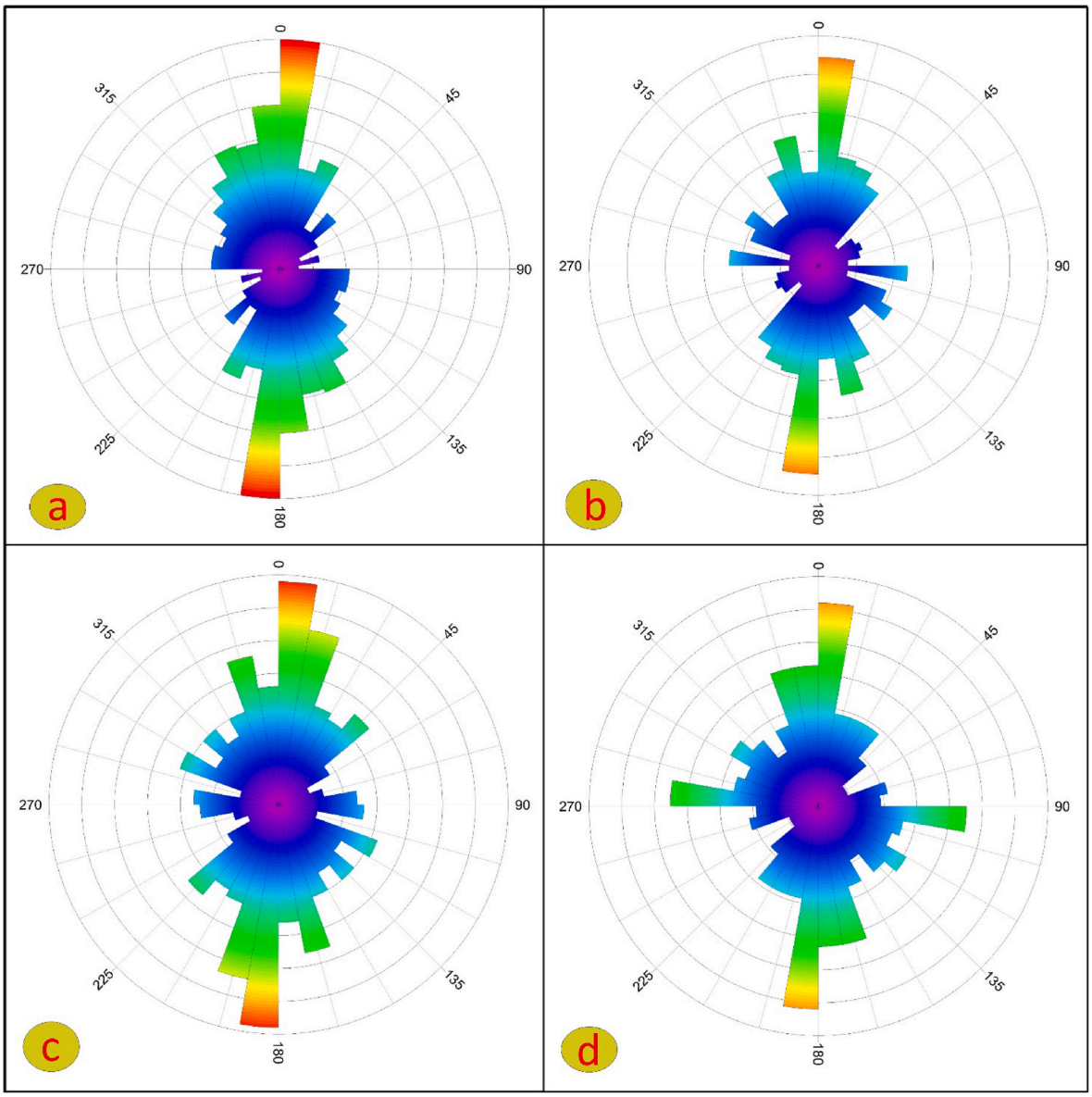

Fig. 8. Rose diagram showing the subsurface structural trends that deduced from the lineament maps (a) 500 m, (b) 1000m, (c) 2000 m, and (d) 3000 m of aeromagnetic data in the study area.

magnetic highs/lows further suggest structural controls, potentially including faults, or lithological contacts with significant magnetic susceptibility contrasts (Elhussein et al., 2024; Holden et al., 2012). Sharp magnetic gradients delineate structural features, notably coinciding with Thrust Faults, Fracture Lineaments, and geologic contacts, indicating susceptibility contrasts arising from fault juxtaposition or lithological boundaries (Hall, 1964). Anomaly morphology further supports geological interpretation: linear highs suggest structurally controlled intrusive bodies (dykes/sills), while circular/irregular highs potentially indicate discrete intrusions (plugs/stocks) or mineralized zones (Ahmed et al., 2020; Elhussein et al., 2024).

The progressive attenuation of high-frequency anomalies and enhancement of regional low-frequency anomalies from UP500 to UP3000 indicate the presence of both shallow and deep magnetic sources with distinct signatures at each level. Well-defined anomalies at lower continuation heights reflect near-surface structures like dikes and intrusions, whereas broader anomalies at higher levels point to deeper tectonic features and basement variations. These maps thus reveal key structural trends and compositional variations critically for understanding the regional geology and targeting mineralization zones and basement structures in the area.

The rose diagrams (Fig. 8) generated from the lineament maps (Fig. 7) reveal variations in structural trends with increasing continuation levels. At 500 m (Fig. 8a), the lineaments show a dominant N-S orientation, indicating that shallow structures such as faults, fractures, and lithological boundaries mainly follow this trend. At 1000 m (Fig. 8b), while the N-S trend remains strong, there is a noticeable increase in NNW-SSE and NE-SW orientations, suggesting the emergence of deeper structural influences and shear zones. Moving to 2000 m (Fig. 8c), the lineament directions remain predominantly N-S but exhibit a more balanced distribution of NE-SW and NNW-SSE trends, implying that multiple intersecting structures control the deeper subsurface geology. At the deepest level, 3000 m (Fig. 8d), the rose diagram highlights both N-S and E-W trends, indicating the presence of significant deep-seated regional lineaments and tectonic boundaries, while the NE-SW trend becomes less pronounced. Overall, this analysis shows that the study area is structurally dominated by N-S trending features across all depths, with NE-SW and NNW-SSE trends gaining prominence at

intermediate levels, and E-W features becoming more visible at greater depths. These variations suggest that shallow structures reflect surface tectonic fabrics, while deeper levels reveal major basement structures and regional tectonic frameworks that are important for understanding geological evolution and identifying mineralization controls within the area. These structural orientations are critical in mineral exploration, as they often serve as conduits for hydrothermal fluid migration and can host vein-type or structurally controlled mineralization, including radioactive (U & Th) and rare earth elements. Mapping these trends at multiple depths enables a more accurate understanding of potential mineralized zones and improves exploration targeting, particularly in structurally complex terrains where mineral deposits are structurally emplaced or reactivated along deep fault zones.

6. Conclusions

The El Maghrabiya- Ria Elgarra magmatic suite, which includes granodiorite, monzogranite, syenogranite, and altered granite, was studied to determine differences in natural radioactivity levels. Measurements with a NaI (Tl) detector found that activity concentrations in granodiorite and monzogranite samples are within globally acceptable limits, whereas syenogranites and altered granites had heightened radioactivity levels that surpass international norms. Granodiorite had the lowest total activity, while altered granites had the greatest (1921.15 ± 844.57 Bqkg^{-1}). These increased values are most likely due to the occurrence of radioactive accessory minerals such zircon, thorite, allanite, and titanite, which contain radionuclides in their crystal structures. To assess potential health concerns, several radiological risk metrics were derived, including the gamma activity index, absorbed dose rate, annual effective dose, excess lifetime cancer risk, and radium equivalent activity. The results show that granodiorite and monzogranite provide little radiation risk, with levels falling within acceptable safety limits. In contrast, syenogranites and altered granites far surpass global safety standards, implying that the increased natural gamma radiation linked to these rocks may constitute a serious health danger, owing to their radioactive material concentration. Integrated aeromagnetic analysis (TMI, RTP, and upward continuation) delineated the subsurface geology and structural framework of the study area. The data revealed pronounced high-amplitude magnetic anomalies spatially correlated with shallow, magnetite-rich granodiorite, metavolcanics, and mapped dikes, contrasting sharply with low-intensity anomalies overlying low-susceptibility felsic rocks and sedimentary cover. Gradient analysis and anomaly morphology further indicated structural controls, with steep magnetic gradients delineating faults, fractures, and lithological contacts. Upward continuation to 0.5 km, 1 km, 2 km, and 3 km progressively attenuated shallow-source anomalies (indicating features like dykes and small intrusions) while enhancing deeper, broader anomalies revealing basement undulations, large intrusions, and regional tectonic trends. Lineament analysis demonstrated a transition from a complex, multi-directional (dominantly N-S) near-surface fracture system at shallow levels to fewer, longer, regionally extensive N-S and NNW-SSE trending crustal-scale structures at depth. Consequently, this study establishes that persistent N-S and NNW-SSE deep-seated lineaments represent primary structural controls and critical targets for structurally controlled mineralization, while the correlation of high-amplitude anomalies with granodiorite and metavolcanics units provides direct vectors for mineral exploration within the area's complex terrain.

CRediT authorship contribution statement

El Saeed R. Lasheen: Writing – review & editing, Writing – original draft, Supervision, Software, Investigation, Formal analysis, Data curation, Conceptualization. **Basma A. El-Badry:** Writing – review & editing, Supervision, Investigation. **Waheed H. Mohamed:** Writing – review & editing, Writing – original draft, Investigation, Data curation. **Ghada A. Khouqeer:** Writing – review & editing, Methodology. **Ioan V. Sanislav:** Writing – review & editing, Supervision. **Mabrouk Sami:** Writing – review & editing, Validation, Supervision.

Availability of data and material

This article contains all of the data examined during this investigation.

Ethical approval

No research with human beings has been carried out by any of the authors of this paper.

Funding

This work was supported and funded by the Deanship of Scientific Research at Imam Mohammad Ibn Saud Islamic University (IMSIU) (grant number IMSIU-DDRSP2502).

Conflict of interest

None.

Appendix A. Supplementary data

Supplementary data to this article can be found online at https://doi.org/10.1016/j.jrras.2025.101910.

References

Abdel-Aal, M. M., Tawfik, F. S., & Kandil, N. M. (2024). Radiation dose assessments for generic nuclear power plants part I: Routine operation. *Applied Radiation and Isotopes, 211*, Article 111412. https://doi.org/10.1016/j.apradiso.2024.111412

Abdel-Hakeem, M., El-Tahir, M., Zeid, E. A., & Rageh, H. (2023). Genetic implications of Th/U, Th/K, and U/K ratios for U mineralizations: A case study from el-missikat and el-erediya shear zones, Eastern Desert, Egypt. *Geochemical Transactions, 24*, 3. https://doi.org/10.1186/s12932-023-00083-3

Abdul Sani, S. F., Muhamad Azim, M. K., Marzuki, A. A., Khandaker, M. U., Almugren, K. S., Daar, E., Alkallas, F. H., & Bradley, D. A. (2022). Radioactivity and elemental concentrations of natural and commercial salt. *Radiation Physics and Chemistry, 190*, Article 109790. https://doi.org/10.1016/j.radphyschem.2021.109790

Aero-Service. (1984). *Final operational report of airborne magnetic/radiation survey in the Eastern Desert, Egypt; for the Egyptian general petroleum corporation (EGPC) and the Egyptian geological survey and mining authority (EGSMA)*. USA: Aero-Service: Houston, TX.

Ahmed, S. B., El Qassas, R. A. Y., & El Salam, H. F. A. (2020). Mapping the possible buried archaeological targets using magnetic and ground penetrating radar data, Fayoum, Egypt. Egypt. J. *Remote Sens. Space Sci., 23*, 321–332. https://doi.org/10.1016/j.ejrs.2019.07.005

Ahmed, S. B., Elhusseiny, A. A., Azzazy, A. A., & El-Qassas, R. A. Y. (2025). Utilization of airborne geophysical data and remote sensing to identify radioactive and hydrothermal alteration zones in the East Qena area, Central Eastern Desert, Egypt. *Acta Geophysica*. https://doi.org/10.1007/s11600-025-01652-z

Akkurt, I., & Günoğlu, K. (2014). Natural radioactivity measurements and radiation dose estimation in some sedimentary rock samples in Turkey. *Science Technology Nuclear install, 2014*, 1–6. https://doi.org/10.1155/2014/950978

Al-Hamarneh, I. F., & Awadallah, M. I. (2009). Soil radioactivity levels and radiation hazard assessment in the highlands of northern Jordan. *Radiation Measurements, 44*, 102–110. https://doi.org/10.1016/j.radmeas.2008.11.005

Al-Mur, B. A., Aljahdali, M. H., Almeelbi, T., & Lasheen, E. S. R. (2025). Spatial radionuclide distribution, mineralogy, and radiological evaluation of the Jeddah shoreline sediments, Red Sea, Saudi Arabia. *Environmental Monitoring and Assessment, 197*, 593. https://doi.org/10.1007/s10661-025-13986-8

AlZahrani, J. H., Alharbi, W. R., & Abbady, A. G. E. (2011). Radiological impacts of natural radioactivity and heat generation by radioactive decay of phosphorite deposits from northwestern Saudi Arabia. *Australian Journal of Basic and Applied Sciences, 5*, 683–690.

Amin, R. M. (2012). Gamma radiation measurements of naturally occurring radioactive samples from commercial Egyptian granites. *Environmental Earth Sciences, 67*, 771–775. https://doi.org/10.1007/s12665-012-1538-x

Attallah, M. F., Hilal, M. A., & Mohamed, Y. T. (2018). Preliminary investigations on reducing the high radiation risk level of TENORM scale waste from petroleum industry. *Radiochimica Acta, 106*, 793–800. https://doi.org/10.1515/ract-2017-2904

Awad, H. A. M., Zakaly, H. M. H., Nastavkin, A. V., & El-Taher, A. (2020). Radiological implication of the granitoid rocks and their associated jasperoid veins, El-Missikat area, Central Eastern Desert, Egypt. *International Journal of Environmental Analytical Chemistry*, 1–14. https://doi.org/10.1080/03067319.2020.1845666

Baranov, V., & Naudy, H. (1964). Numerical calculation of the formula of reduction to the magnetic pole. *Geophysics, 29*, 67–79.

Elhussein, M., Barakat, M. K., Alexakis, D. E., Alarifi, N., Mohamed, E. S., Kucher, D. E., Shokr, M. S., & Youssef, M. A. S. (2024). Aeromagnetic data analysis for sustainable structural mapping of the missiakat Al jukh area in the central Eastern Desert: Enhancing resource exploration with minimal environmental impact. *Sustainability, 16*, 8764. https://doi.org/10.3390/su16208764

Eshanibli, A. (2020). Structural interpretation of the gravity and magnetic data in the ajdabiya trough, sirt basin. *Libya*. https://doi.org/10.13140/RG.2.2.33695.47522/1

Eshanibli, A. S., Osagie, A. U., Ismail, N. A., & Ghanush, H. B. (2021). Analysis of gravity and aeromagnetic data to determine structural trend and basement depth beneath the Ajdabiya Trough in northeastern Libya. *SN Applied Sciences, 3*, 228. https://doi.org/10.1007/s42452-021-04263-7

European Commission. (1999). Radiological protection principles concerning the natural radioactivity of building materials. Radiation Protection 112, Directorate General Environment. *Nuclear safety and civil protection*. European Commission.

Fathy, D., Zakaly, H. M. H., Lasheen, E. S. R., Elsaman, R., Alarifi, S. S., Sami, M., Awad, H. A., & Ene, A. (2023). Assessing geochemical and natural radioactivity impacts of Hamadat phosphatic mine through radiological indices. *PLoS One, 18*, Article e0287422. https://doi.org/10.1371/journal.pone.0287422

Freitas, A. C., & Alencar, A. S. (2004). Gamma dose rates and distribution of natural radionuclides in sand beaches—ilha Grande, Southeastern Brazil. *Journal of Environmental Radioactivity, 75*, 211–223. https://doi.org/10.1016/j.jenvrad.2004.01.002

Guillén, J., Tejado, J. J., Baeza, A., Salas, A., & Muñoz-Muñoz, J. G. (2014). Environmental impact of a granite processing factory as source of naturally occurring radionuclides. *Applied Geochemistry, 47*, 122–129. https://doi.org/10.1016/j.apgeochem.2014.06.001

Hall, D. H. (1964). *Magnetic and tectonic regionalization on texada island British Colombia* (Vol. 29, pp. 566–581).

Hamimi, Z., Eldosouky, A. M., Hagag, W., & Kamh, S. Z. (2023). Large-scale geological structures of the Egyptian nubian shield. *Scientific Reports, 13*. https://doi.org/10.1038/s41598-023-29008-x

Hao, M., Zhang, F., Tai, Z., Du, W., Ren, L., & Li, Y. (2018). Reduction to the pole at low latitudes by using the Taylor series iterative method. *Journal of Applied Geophysics, 159*, 127–134. https://doi.org/10.1016/j.jappgeo.2018.08.004

Holden, E.-J., Wong, J. C., Kovesi, P., Wedge, D., Dentith, M., & Bagas, L. (2012). Identifying structural complexity in aeromagnetic data: An image analysis approach to greenfields gold exploration. *Ore Geology Reviews, 46*, 47–59. https://doi.org/10.1016/j.oregeorev.2011.11.002

Kanmi, A. S., Ibrahim, U., Goki, N. G., Rilwan, U., Sayyed, M. I., Maghrbi, Y., Namq, B. F., Najam, L. A., & Wais, T. Y. (2025). Assessment of natural radioactivity and its radiological risks in the soil of local government areas (asa, ilorin east, ilorin south, irepodun, moro, and oyun) in kwara state, Nigeria. *Case Studies in Chemical and Environmental Engineering, 11*, Article 101040. https://doi.org/10.1016/j.cscee.2024.101040

Khaleal, F. M., Tahoon, M. A., Saleh, G. M., Kamar, M. S., Zakaly, H. M. H., Zidan, I. H., Al-Mur, B. A., Alarif, S. S., & Lasheen, E. S. R. (2023). Dolphin-shaped island: Exploring the natural resources and radiological hazards of Wadi El gemal island. *Marine Pollution Bulletin, 194*, Article 115367. https://doi.org/10.1016/j.marpolbul.2023.115367

Khalifa, M. M., Mohamed, W. H., El Ammawy, M. A., Taha, A. I., Awad, A., & Orchid, A. A. (2024). Evaluation of the subsurface structural features of the Farafra Oasis, western desert, Egypt using aeromagnetic data. *Model. Earth Syst. Environ., 10*, 723–733. https://doi.org/10.1007/s40808-023-01806-2

Khan, M., Li, H., Algeo, T. J., Khan, A., Förster, M. W., & Ullah, Z. (2025). Geochemistry and geochronology of A-type intermediate-felsic rocks in NW himalaya, Pakistan: Implications for petrogenesis and tectonic evolution of northern gondwana. *Geochemistry, Geophysics, Geosystems, 26*, Article e2024GC011802. https://doi.org/10.1029/2024GC011802

Khandaker, M. U., Mahmud, A., Siraz, M. M. M., Alam, M. S., Trishna, J. M., Rashid, M. B., Hussin, F., Kassim, M. A., & Osman, H. (2025). Identification of elevated level background radiation areas, exposure scenarios and implications for public health and environmental safety in Malaysia: A comprehensive study. *Radiation Physics and Chemistry, 235*, Article 112851. https://doi.org/10.1016/j.radphyschem.2025.112851

Krebs, M. Y., Pearson, D. G., Fagan, A. J., Bussweiler, Y., & Sarkar, C. (2019). The application of trace elements and Sr–Pb isotopes to dating and tracing ruby formation: The Aappaluttoq deposit, SW Greenland. *Chemical Geology, 523*, 42–58. https://doi.org/10.1016/j.chemgeo.2019.05.035

Kumar, N., Khyalia, B., Yadav, J., Singh, B., Gupta, V., Singh, P. P., Singh, H., & Dalal, R. (2024). Assessment of natural radioactivity in soil around Khetri copper belt of Rajasthan, India. *Journal of Radioanalytical and Nuclear Chemistry, 333*, 3185–3194. https://doi.org/10.1007/s10967-023-09301-9

Kuzmanović, P., Filipović Petrović, L., Petrović, J., Forkapić, S., Hansman, J., Velimirović, D., & Knežević Radić, J. (2024). Physico-chemical, technological and radiological characteristics of kaolinized granite from northwestern Serbia. *Radiation Physics and Chemistry, 222*, Article 111885. https://doi.org/10.1016/j.radphyschem.2024.111885

Lasheen, E. S. R., Abart, R., Ahmed, M. S., Abdelfadil, K. M., Farahat, E. S., & Sami, M. (2025). Petrological constraints of the Ediacaran magmatic intrusions, Homrit Mukpid area, southeastern Desert, Egypt: Bulk rock geochemistry and mineralogy. *Journal of African Earth Sciences, 225*, Article 105567. https://doi.org/10.1016/j.jafrearsci.2025.105567

Lasheen, E. S. R., Rashwan, M. A., & Azer, M. K. (2023). Effect of mineralogical variations on physico-mechanical and thermal properties of granitic rocks. *Scientific Reports, 13*, Article 10320. https://doi.org/10.1038/s41598-023-36459-9

Lasheen, E. S. R., Rashwan, M. A., Osman, H., Alamri, S., Khandaker, M. U., & Hanfi, M. Y. (2021). Radiological hazard evaluation of some Egyptian magmatic rocks used as ornamental stone: Petrography and natural radioactivity. *Materials, 14*, 7290. https://doi.org/10.3390/ma14237290

Lasheen, E. S. R., Sami, M., Hegazy, A. A., Arman, H., Sanislav, I. V., Ahmed, M. S., & Rashwan, M. A. (2024). Petrological characteristics and physico-mechanical properties of dokhan Volcanics for decorative stones and building material applications. *Buildings, 14*, 3418. https://doi.org/10.3390/buildings14113418

Lei, B., Zhao, L., Girault, F., Cai, Z., Luo, C., Thapa, S., She, J., & Perrier, F. (2023). Overview and large-scale representative estimate of radon-222 flux data in China. *Environmental Advances, 11*, Article 100312. https://doi.org/10.1016/j.envadv.2022.100312

Li, J., Liu, S., Zhang, Y., Chen, L., Yan, Y., Cheng, W., Lou, H., & Zhang, Y. (2015). Pre-assessment of dose rates of 134Cs, 137Cs, and 60Co for marine biota from discharge of Haiyang Nuclear Power Plant, China. *Journal of Environmental Radioactivity, 147*, 8–13. https://doi.org/10.1016/j.jenvrad.2015.05.001

Li, H., Wang, Q., Zhang, C., Su, W., Ma, Y., Zhong, Q., Xiao, E., Xia, F., Zheng, G., & Xiao, T. (2024). Geochemical distribution and environmental risks of radionuclides in soils and sediments runoff of a uranium mining area in south China. *Toxics, 12*, 95. https://doi.org/10.3390/toxics12010095

O'Brien, K., & Sanna, R. (1976). The distribution of absorbed dose-rates in humans from exposure to environmental gamma rays. *Health Physics, 30*(1), 71–78.

Osinowo, O. O., & Taiwo, T. O. (2020). Analysis of high-resolution aeromagnetic (HRAM) data of Lower Benue Trough, Southeastern Nigeria, for hydrocarbon potential evaluation. *NRIAG J. Astron. Geophys., 9*, 350–361. https://doi.org/10.1080/20909977.2020.1746890

Özden, S., & Aközcan, S. (2021). Natural radioactivity measurements and evaluation of radiological hazards in sediment of Aliağa Bay, İzmir (Turkey). *Arabian Journal of Geosciences, 14*, 64. https://doi.org/10.1007/s12517-020-06446-9

Özden, S., Pehlivanoğlu, S. A., & Günay, O. (2023). Evaluation of natural radioactivity in soils of Konya (Turkey) and estimation of radiological health hazards. *Environmental Monitoring and Assessment, 195*, 1523. https://doi.org/10.1007/s10661-023-12162-0

Pavlidou, S., Koroneos, A., Papastefanou, C., Christofides, G., Stoulos, S., & Vavelides, M. (2006). Natural radioactivity of granites used as building materials. *Journal of Environmental Radioactivity, 89*, 48–60. https://doi.org/10.1016/j.jenvrad.2006.03.005

Phillips, J. D. (2007). *Geosoft executables _GX's_ developed by the U.S. Geological Survey, version 2.0 with notes on GX development from FORTRAN code*. U.S. Geological Survey Open-File Report (Open-File Report). Open-File Report.

Qureshi, A. A., Tariq, S., Din, K. U., Manzoor, S., Calligaris, C., & Waheed, A. (2014). Evaluation of excessive lifetime cancer risk due to natural radioactivity in the rivers sediments of Northern Pakistan. *Journal Radiata Research Applied Scientific, 7*, 438–447. https://doi.org/10.1016/j.jrras.2014.07.008

Raghavendra, T., Vishwaprasad, K., Kalyani, G., Vijayalakshmi, T., Himabindu, V., Arunachalam, J., Padmasavithri, P., Kumar, V., & Tripathi, R. M. (2019). Assessment of natural radioactivity in soils around the proposed uranium mining site of lambapur – peddagattu and seripally, India. *Journal of the Geological Society of India, 93*, 223–227. https://doi.org/10.1007/s12594-019-1156-2

Ramola, R. C., Choubey, V. M., Prasad, G., Gusain, G. S., Tosheva, Z., & Kies, A. (2011). Radionuclide analysisin the soil of Kumaun Himalaya, India, using gamma ray spectrometry. *Current Science, 100*, 6–25.

Ravisankar, R., Chandramohan, J., Chandrasekaran, A., Prince Prakash Jebakumar, J., Vijayalakshmi, I., Vijayagopal, P., & Venkatraman, B. (2015). Assessments of radioactivity concentration of natural radionuclides and radiological hazard indices in sediment samples from the East coast of Tamilnadu, India with statistical approach. *Marine Pollution Bulletin, 97*, 419–430. https://doi.org/10.1016/j.marpolbul.2015.05.058

Sahoo, S. K., Hosoda, M., Kamagata, S., Sorimachi, A., Ishikawa, T., Tokonami, S., & Uchida, S. (2011). Thorium, uranium and rare earth elements concentration in weathered Japanese soil samples. *Progreso Nuclear Science Technology, 1*, 416–419. https://doi.org/10.15669/pnst.1.416

Saleh, G. M., Kamar, M. S., Khaleal, F. M., Azer, M. K., Nasr, T., & Lasheen, E. S. R. (2025a). Petrogenesis and tectonic evolution of tourmaline- bearing leucogranites, Sikait area, Southeastn desert of Egypt utilizing mineralogical and bulk rock analysis. *Scientific Reports, 15*, Article 20191. https://doi.org/10.1038/s41598-025-06155-x

Saleh, G. M., Kamh, S. Z., Abdalla, F., Kilias, A., & Lasheen, E. S. R. (2024). A new occurrence of rift-related damtjernite (ultramafic) lamprophyre, Gebel Anweiyib area, Arabian Nubian shield: Insights from bulk rock geochemistry and remote sensing data analysis. *Physics and Chemistry of the Earth, Parts A/B/C, 133*, Article 103530. https://doi.org/10.1016/j.pce.2023.103530

Saleh, G. M., Lasheen, E. S. R., Foi, M., Abdalla, F., & Abdelaal, A. (2025b). Assessment of radioactivity and heavy metal pollution levels in the coastal sediments in the red sea region of Sharm El Luli, Egypt. *Water, Air, and Soil Pollution, 236*, 319. https://doi.org/10.1007/s11270-025-07962-8

Sayyed, M. I., Maria, Z. M., Hussein, Z. A., Najam, L. A., Namq, B. F., Wais, T. Y., Mostafa, M. Y. A., & Mansour, H. (2024). Radiological hazard assessment of soil from Kasik oil refinery, Nineveh, Iraq. *Nuclear Engineering and Technology, 56*, 4782–4790. https://doi.org/10.1016/j.net.2024.06.041

Senthilkumar, G., Raghu, Y., Sivakumar, S., Chandrasekaran, A., Prem Anand, D., & Ravisankar, R. (2014). Natural radioactivity measurement and evaluation of radiological hazards in some commercial flooring materials used in Thiruvannamalai, Tamilnadu, India. *Journal Radiata Research Applied Scientific, 7*, 116–122. https://doi.org/10.1016/j.jrras.2013.12.009

Shahrokhi, A., Adelikhah, M., Chalupnik, S., Kocsis, E., Toth-Bodrogi, E., & Kovács, T. (2020). Radioactivity of building materials in Mahallat, Iran – an area exposed to a high level of natural background radiation – attenuation of external radiation doses. *Materiales de Construcción, 70*, 233. https://doi.org/10.3989/mc.2020.03820

Sharaf, J. M., & Hamideen, M. S. (2013). Measurement of natural radioactivity in Jordanian building materials and their contribution to the public indoor gamma dose rate. *Applied Radiation and Isotopes, 80*, 61–66. https://doi.org/10.1016/j.apradiso.2013.06.016

Shehzad, W., Satti, K. H., Khan, M., Khan, K., Naseem, A., Ur Rehman, S., & Jabbar, A. (2019). Estimation of background radiation levels and associated health risks in mineral rich district Chiniot, Pakistan. *Journal of Radioanalytical and Nuclear Chemistry, 319*, 1051–1058. https://doi.org/10.1007/s10967-019-06425-9

Shereif, A. S., Shebl, A., Abdellatif, M., Abdelkader, M. A., Badawi, M., Mahmoud, A. S., & Csámer, Á. (2025). Integrated remote sensing and geophysical data for delineating the radioactive mineralization bearing-alteration zones, El-Missikat and El-Erediya areas, Central Eastern Desert, Egypt. *Remote Sensing Applications: Society and Environment., 38*, Article 101624. https://doi.org/10.1016/j.rsase.2025.101624

Sivakumar, S., Chandrasekaran, A., Senthilkumar, G., Suresh Gandhi, M., & Ravisankar, R. (2018). Determination of radioactivity levels and associated hazards of coastal sediment from south east coast of Tamil Nadu with statistical approach. *Iranian Journal of Science Transactions Science, 42*, 601–614. https://doi.org/10.1007/s40995-017-0184-2

Stern, R. J. (2018). Neoproterozoic formation and evolution of Eastern Desert continental crust – the importance of the infrastructure-superstructure transition. *Journal of African Earth Sciences, 146*, 15–27. https://doi.org/10.1016/j.jafrearsci.2017.01.001

Taskin, H., Karavus, M., Ay, P., Topuzoglu, A., Hidiroglu, S., & Karahan, G. (2009). Radionuclide concentrations in soil and lifetime cancer risk due to gamma radioactivity in Kirklareli, Turkey. *Journal of Environmental Radioactivity, 100*, 49–53. https://doi.org/10.1016/j.jenvrad.2008.10.012

Tuo, F., Peng, X., Zhou, Q., & Zhang, J. (2020). Assessment of natural radioactivity levels and radiological hazards in building materials. *Radiation Protection Dosimetry, 188*, 316–321. https://doi.org/10.1093/rpd/ncz289

UNSCEAR. (2000). *Sources and effects of ionizing radiation: United nations scientific committee on the effects of atomic radiation: UNSCEAR 2000 report to the general assembly, with scientific annexes* (Ed). New York: United Nations.

UNSCEAR. (2010). *Sources and effects of ionizing radiation: United nations scientific committee on the effects of atomic radiation: UNSCEAR 2008 report to the general assembly, with scientific annexes* (Ed). New York: United Nations.

Vukasinovic, I., Djordjevic, A., Rajkovic, M., Todorovic, D., & Pavlovic, V. (2010). Distribution of natural radionuclides in anthrosol-type soil. *Turkish Journal of Agriculture and Forestry*. https://doi.org/10.3906/tar-0911-59

Wais, T. Y., Ali, F. N. M., Najam, L. A., Mansour, H., & Mostafa, M. Y. A. (2023). Assessment of natural radioactivity and radiological hazards of soil collected from rabia town in nineveh governorate (North Iraq). *Physica Scripta, 98*, Article 065304. https://doi.org/10.1088/1402-4896/acd732

Wais, T. Y., Namq, B. F., Najam, L. A., Khalaf, H. N. B., Gismelseed, A. M., Mansour, H., & Mostafa, M. Y. A. (2025). Natural and artificial radioactivity levels in the agricultural soil of lands near the Al-Kasak oil refinery, northern Iraq. *Journal of Radioanalytical and Nuclear Chemistry, 334*, 1471–1484. https://doi.org/10.1007/s10967-024-09912-w

Yıldırım, A., & Gülmez, F. (2025). Natural radioactivity and radiological hazards in ultrapotassic rocks from the Central Pontides, Türkiye. *Annals of Nuclear Energy, 223*, Article 111619. https://doi.org/10.1016/j.anucene.2025.111619

Yu, K. N., Young, E. C. M., Stokes, M. J., Luo, D. L., & Zhang, C. X. (1992). Indoor radon and environmental gamma radiation in Hong Kong. *Radiation Protection Dosimetry, 40*, 259–263. https://doi.org/10.1093/oxfordjournals.rpd.a081212

Yuan, J.-M., Wang, Q.-S., Ross, R., Henderson, B., & Yu, M. (1995). Diet and breast cancer in Shanghai and Tianjin, China. *British Journal of Cancer, 71*, 1353–1358. https://doi.org/10.1038/bjc.1995.263

Zakaly, H. M. H., Awad, H. A., Lasheen, E. S. R., Issa, S. A. M., Elsaman, R., Khandaker, M. U., Al-awah, H., Fathy, D., & Sami, M. (2024). Radiometric and petrographic characterization of El-Yatima granite: Evaluating radiological risks and mineralogical features. *Radiation Physics and Chemistry, 224*, Article 111992. https://doi.org/10.1016/j.radphyschem.2024.111992

Zhdanov, M. S. (2015). Migration of 3-D gravity, gravity tensor, and total magnetic intensity data. In *Inverse theory and applications in geophysics* (pp. 261–281). Elsevier. https://doi.org/10.1016/B978-0-444-62674-5.00011-6.